

LYRA OBSERVATIONS OF TWO OSCILLATION MODES IN A SINGLE FLARE

T. VAN DOORSSLAERE^{1,5}, A. DE GROOF², J. ZENDER³, D. BERGHMANS⁴, AND M. GOOSSENS¹

¹ Centre for Plasma Astrophysics, Department of Mathematics, Katholieke Universiteit Leuven, Celestijnenlaan 200B bus 2400, B-3001 Heverlee, Belgium; Tom.VanDoorsselaere@wis.kuleuven.be

² ESA, Science & Robotic Exploration Department, c/o Royal Observatory of Belgium, Ringlaan 3, B-1180 Brussels, Belgium

³ ESA Research and Scientific Support Department, ESTEC, NL-2200 AG Noordwijk, The Netherlands

⁴ Royal Observatory of Belgium, Ringlaan 3, B-1180 Brussels, Belgium

Received 2011 April 15; accepted 2011 July 26; published 2011 October 3

ABSTRACT

We analyze light curves from the LYRA irradiance experiment on board *PROBA2* during the flare of 2010 February 8. We see both long- and short-period oscillations during the flare. The long-period oscillation is interpreted in terms of standing slow sausage modes; the short-period oscillation is thought to be a standing fast sausage mode. The simultaneous presence of two oscillation modes in the same flaring structure allows for new coronal seismological applications. The periods are used to find seismological estimates of the plasma- β and the density contrast of the flaring loop. Also the wave mode number is estimated from the observed periods.

Key words: Sun: corona – Sun: flares – Sun: oscillations

Online-only material: color figures

1. INTRODUCTION

Oscillations have been frequently observed in solar flares, and are often called quasi-periodic pulsations (QPPs; for a recent review, see Nakariakov & Melnikov 2009). They can be observed as periodic intensity increases and decreases during a solar flare in a wide range of wavelengths: X-rays (e.g., Asai et al. 2001), white light (e.g., McAteer et al. 2005), microwaves (e.g., Inglis & Nakariakov 2009), and recently even in γ -rays (Nakariakov et al. 2010).

In their review, Nakariakov & Melnikov (2009) argue that the QPPs may be split into short-period and long-period regimes. The short-period oscillations are often attributed to electromagnetic, plasma, or whistler waves in the accelerated flare electron medium. The long-period oscillations are most often believed to be connected to MHD processes. This is confirmed by the observations of Zimovets & Struminsky (2009), where simultaneously to the QPP, systematic oscillations are observed in the EUV emission of the post-flare loops.

The excitation mechanism for QPPs has not been conclusively identified yet. Three possibilities have been suggested: the flare itself is intermittent or “quasi-periodic” (e.g., Bárta et al. 2008), the flare is periodically driven by an external oscillation (e.g., Nakariakov et al. 2006), or the post-flare loop that guides the energetic particles from the coronal flare site to the photosphere is impulsively excited (e.g., Fletcher & Hudson 2008). The latter case opens up interesting avenues to perform coronal seismology, and thus to measure local physical parameters in the immediate flare surroundings. In that case, the oscillations are usually interpreted as the fast sausage mode (Melnikov et al. 2005), the standing slow mode (Mariska 2005), or the fast kink mode (Inglis & Nakariakov 2009). The fast sausage mode and the standing slow mode are the most invoked interpretations, because these oscillation modes are the only ones with a significant compressibility (showing as observed intensity perturbations) in a simple magnetic cylinder model (e.g., Edwin & Roberts 1983).

The term “sausage” refers to axisymmetric motions ($\partial/\partial\varphi$ or the azimuthal wavenumber $m = 0$).

Coronal seismology (for a review, see Nakariakov & Verwichte 2005) is the branch of solar physics in which observations of waves are compared to the computed versions for specified plasma structures. Adjustment of the model parameters to match the observations then leads to remote sensing of plasma parameters, which are difficult to measure otherwise. Coronal seismology has been quite successfully applied in the last decade, and has been used to measure the magnetic field (Nakariakov & Ofman 2001), the radial loop structuring (Goossens et al. 2002, 2008; Aschwanden et al. 2003; Van Doorsselaere et al. 2008), the density stratification along the loop (Andries et al. 2005a), Alfvén transit times (Arregui et al. 2007), and recently the polytropic index and thermal conduction coefficient (Van Doorsselaere et al. 2011).

As for all seismological applications, it is of great importance to measure multiple modes, because this allows the equilibrium parameters to be restricted much more precisely. In coronal seismology, this has only been possible to a limited extent, because coronal MHD oscillations turn out to be heavily damped and thus no high spectral resolution may be obtained. In 2004, Verwichte et al. were the first to detect a higher harmonic in transverse loop oscillations, enabling better seismology (Andries et al. 2005b, 2009). This was later followed up by the detection of three modes (De Moortel & Brady 2007; Van Doorsselaere et al. 2009), but the measurement uncertainties for the shortest period are too high to perform seismology. For prominences, the situation is entirely different: many oscillation modes have been observed (Régner et al. 2001; Pouget et al. 2006), making mode identification difficult.

The seismology of QPPs is very promising. The instruments observing these oscillations (irradiance experiments, radio telescopes) have a superior time cadence, but have only limited spatial resolution. The fact that the strong flaring emission is generated in a small volume around the flare provides a naturally fine spatial resolution. Up to now, the seismology of QPPs has been difficult because of the unknown geometry of the oscillating region and the unknown nature of the QPPs.

⁵ T.V.D. is a post-doctoral fellow of the FWO-Vlaanderen.

In this paper, we report the detection of the simultaneous occurrence of two different modes, a standing slow mode and a fast sausage mode, in a flare observed with *PROBA2*/LYRA. In order to extract estimates for plasma parameters from the observations, we assume a loop geometry that guides the observed oscillations.

2. OBSERVATIONS AND RESULTS

The data used in this study are acquired using the *PROBA2* satellite (Gantois et al. 2010). LYRA (Hochedez et al. 2006; Benmoussa et al. 2009) is a radiometer aboard *PROBA2* that measures the total solar irradiance (without spatial resolution) with a 20 Hz cadence in four different channels: aluminum, zirconium, Ly α , and Herzberg. The first two channels mainly measure the emission from the corona. The Ly α channel measures the chromospheric radiation, while the Herzberg channel focuses on the continuum emission. The aluminum channel has a wavelength range between 17 nm and 80 nm with a contribution from wavelengths below 5 nm (and includes the He II emission), while the zirconium channel observes between wavelengths of 6 nm and 20 nm, with a hot component below 2 nm (and excludes the He II emission). The Ly α channel has a narrow wavelength focus: 120–123 nm. The Herzberg continuum channel has a response function between 190 nm and 220 nm.

We study the M class flare of 2010 February 8 between 13:40UT and 13:54UT. The EUV imager on board *PROBA2*, SWAP (Halain et al. 2010), shows no other flares during the time interval studied,⁶ indicating that the oscillations are not triggered by an external cause. The intensity evolution during the flare is shown in Figure 1 for three of the four LYRA channels and the *GOES* data. For reasons explained later, we take $t_0 = 49448.043$ s (13:44:08.04UT). The time series is cut off at $t = t_0 + 591.90$ s in order to avoid the subsequent spacecraft large-angle rotation (LAR). Visual inspection of the data already shows a clear periodicity, especially in the Ly α filter. In the data, periodic intensity peaks are visually observed at 10 s, 60 s, and 120 s (not so visible in Figure 1).

2.1. Long-period Oscillations

In order to study these oscillations, the long-term trend needs to be removed. This is done by using a running average with a 75 s window (i.e., the IDL `smooth` command with a spacing of 1500 data points). We have used different lengths for the averaging window (65 s–80 s) to obtain an identical result. The results of this trend removal are shown as the relative intensity in Figure 2. It is obvious from Figures 1 and 2 that the trend has not been removed properly at the start of the flare, especially in the zirconium and aluminum channels. This is evidenced by the large minimum around -25 s and maximum at 40 s. It is important that this minimum is excluded from the period analysis to avoid periodicities introduced by the incorrect trend subtraction. Thus we take $t_0 = 49448.043$ s (13:44:08.04UT) as the starting point of the time series. For the period analysis, the time series has been truncated at $t_e = t_0 + 441.911$ s = 49889.954 s (13:51:29.95UT).

The power spectrum (Fourier transform) of the relative signals (Figure 2) is shown in Figure 3. The spectrum for all three channels shows a significant peak. We find a period of 63 s for

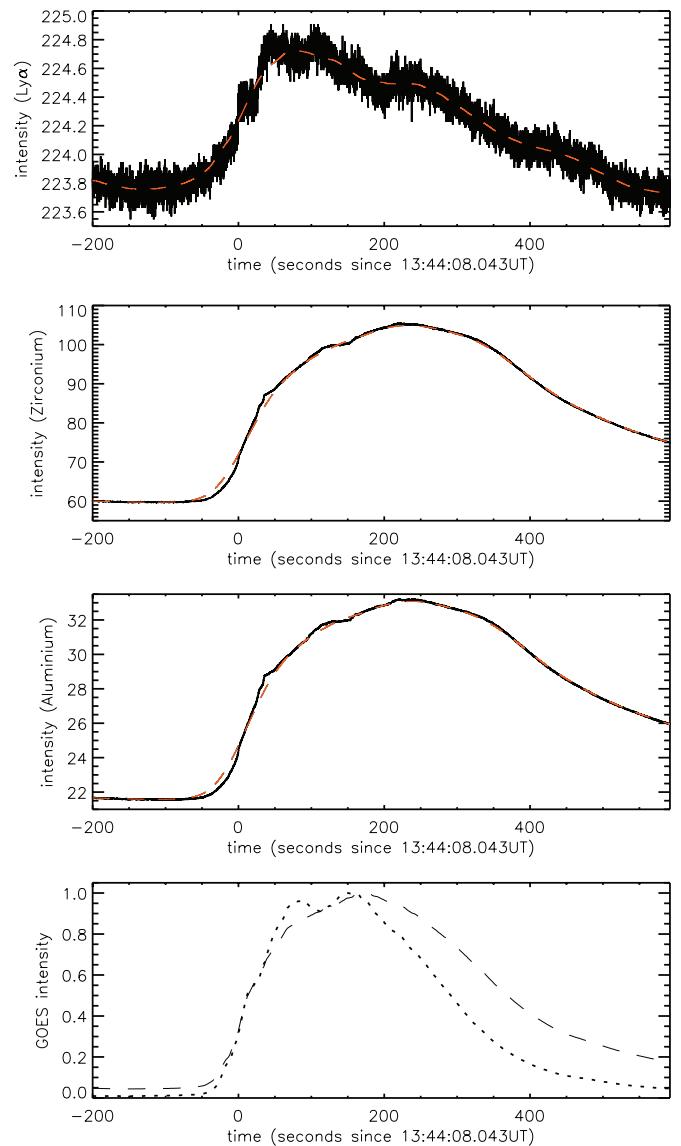


Figure 1. Top three panels are the LYRA intensity curves for the M2.0 flare on 2010 February 8. The horizontal axis is time (in seconds since t_0) and the vertical axis is intensity (in kHz). Intensity in the Ly α , zirconium, and aluminum channels are shown, respectively, in panels 1, 2, and 3 from top to bottom. In those panels, the dashed line is the long-term trend that has been used for background subtraction. The bottom panel shows the normalized *GOES* intensity curves for the same period of time. The short-wavelength data (0.05–0.4 nm) are shown as a dotted line; the long-wavelength data (0.1–0.8 nm) are plotted with a dashed line.

(A color version of this figure is available in the online journal.)

the Ly α channel, 74 s for the aluminum channel, and 88 s for the zirconium channel. While the differences between the periods of different channels may seem large, they are only one frequency resolution step ($(\text{length of time series})^{-1}$) separated. As such, one may say that these periods are equal, and the differences are within the uncertainties of the Fourier transform.

To check whether these spectral peaks actually correspond to physical oscillations, we have filtered the signal with a top hat frequency profile between 10 mHz and 19 mHz. This filter is shown in Figure 3. The filtered signal is then overplotted on the relative signal. This is shown in Figure 4. It is clear that the spectral peak corresponds to the visually identified oscillation. The filtered signal matches rather well with the relative intensity signal.

⁶ http://proba2.sidc.be/swap/data/mpg/movies/2010/02/20100208_swap_movie.mp4

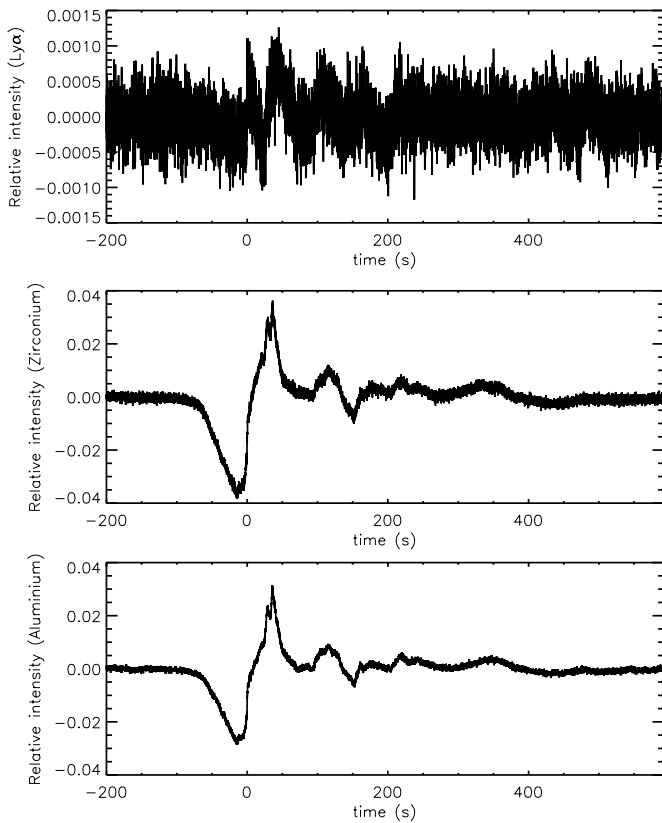


Figure 2. Relative intensity δI (vertical axis) vs. time (horizontal axis) during the same time window as Figure 1. The long-term trend has been removed and used as normalization, i.e., $\delta I = \frac{I - I_{\text{trend}}}{I_{\text{trend}}}$. Again, from top to bottom we have Ly α , zirconium, and aluminum filters.

2.2. Short-period Oscillations

We repeat the same analysis, but now we remove the trend by smoothing over a window of 250 data points (i.e., a window of 12.5 s). We also restrict the analysis to the zirconium and Ly α channels, because the aluminum channel gives qualitatively the same results as the zirconium channel. The Herzberg channel shows no oscillatory power and is not shown. This window for the sliding average is chosen to bring out the rapid oscillations that have been visually identified in the raw time series. They are not visible in Figure 1, though.

After the removal of the trend, a Fourier spectrum is constructed, which is shown in Figure 5. Both the spectrum from the Ly α signal and the zirconium channel show a clear peak around 117 mHz, corresponding to a period of 8.5 s. Once again, we confirm the relevance and significance of this spectral peak by filtering the de-trended signal with a top hat frequency filter (with a spectral window from 107 mHz to 127 mHz), and overplotting the result on the signal. This is shown in Figure 6. It is obvious that the short-period oscillation is present in both signals during the rising phase of the flare (left panels). In Ly α the maximum of the flare occurs between $t = 50$ s and $t = 100$ s. In zirconium, the maximum of the flare occurs around $t = 230$ s. This shift of the maxima between these two channels has been observed before (Neupert effect; see, e.g., Veronig et al. 2005, and references therein). This is usually interpreted by assuming a thick-target collision of the flare energetic particles with the dense chromosphere (Ly α emission), of which the heat is used to evaporate chromospheric material to fill the post-flare loops (emitting at coronal temperatures).

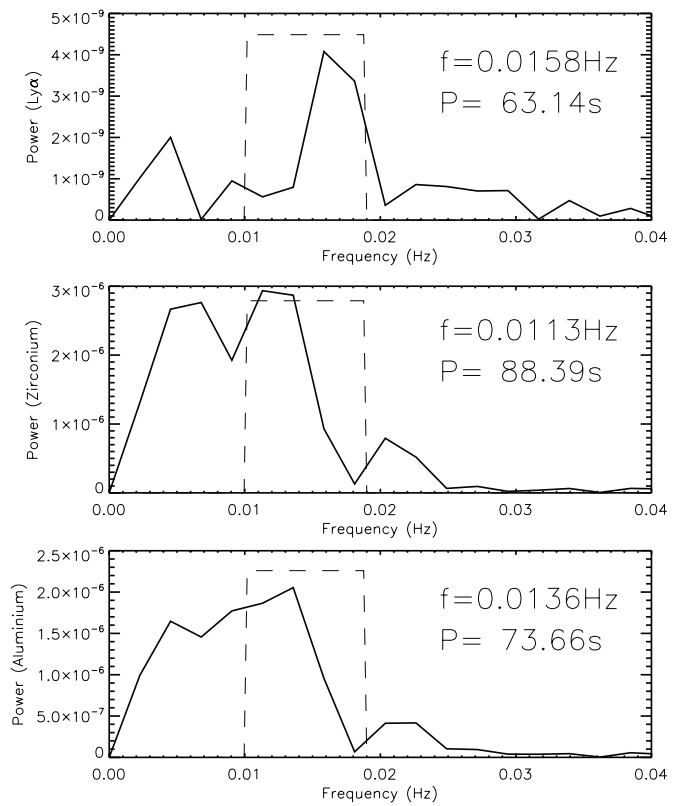


Figure 3. Fourier transforms of the relative signals shown in Figure 2. The horizontal axis is frequency (Hz), while the vertical axis is power. The frequency and period of maximum power are printed in the top right of each panel. From top to bottom: Ly α , zirconium, and aluminum signals. The dashed lines indicate the spectral window used for filtering the signal (see Figure 4).

After $t = 60$ s (close to the Ly α flare peak), the oscillation signal in the zirconium channel seems to damp away. On the other hand, it does not damp away in the Ly α signal. This is made even more clear in the right panels of Figure 6, during the decaying phase of the flare. While the 8.5 s periodicity is still observed in the Ly α channel, there is hardly any oscillatory power in the zirconium channel. The presence of oscillations in the rising phase of a flare and absence during the decaying phase has been reported before by Fárník et al. (2003). However, no conclusive model has been formulated for the appearance of waves during the rising phase of the flare, which rapidly decay after the flare maximum.

Both the long- and short-period oscillations can also be found in the *GOES* light curves using the same data analysis techniques, excluding the possibility of instrumental effects.

3. SEISMOLOGY

As mentioned in the introduction, several mechanisms have been proposed to explain the QPPs. They could be caused by an external driver of reconnection, by bursty reconnection, or by an oscillating post-flare loop. Since it is unclear how the former two mechanisms would introduce multiperiodicity in the light curve, we concentrate on the latter mechanism. Of course, we cannot rule out that the two observed periods are each caused by a different mechanism.

As a basic (standard) model for solar coronal loop oscillations, we take a magnetic-field-aligned cylinder that is denser than the surroundings (for a diagram, see Figure 2 of Nakariakov & Verwichte 2005). In such a model, several modes

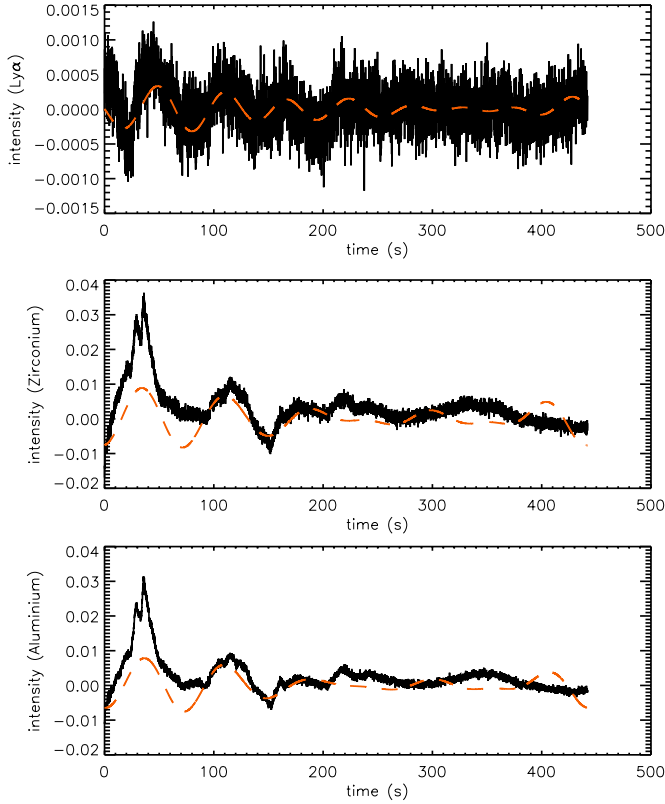


Figure 4. Black line is the relative signal (as in Figure 2). The dashed orange line is the relative intensity signal filtered with a top hat window between 10 mHz and 19 mHz. From top to bottom: Ly α , zirconium, and aluminum signals. (A color version of this figure is available in the online journal.)

occur, most of which have been observed in the corona. The azimuthal wavenumber m drastically influences the nature of these modes. For $m = 1$, we have the antisymmetric (with respect to the cylinder axis) fast kink mode, which is a nearly incompressible mode manifested as transverse displacement of the cylinder. It operates on an Alfvén timescale. For $m = 0$,

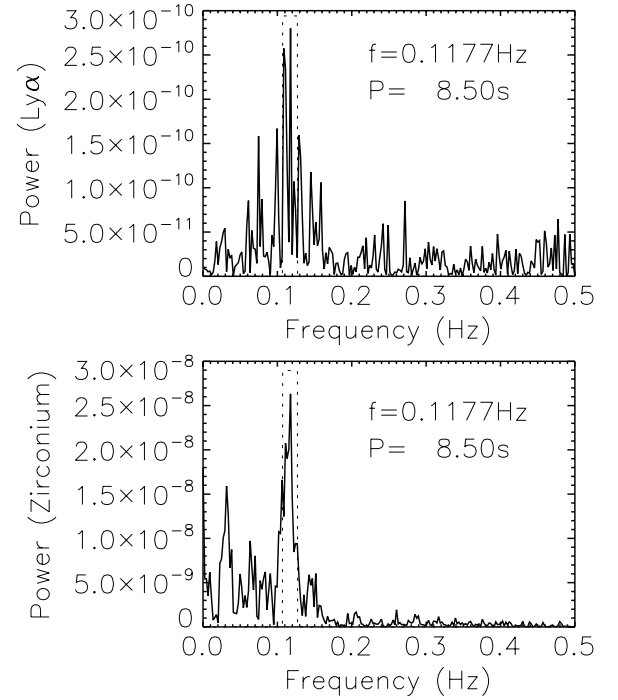


Figure 5. Fourier spectra for the short-period oscillations, with the frequency as the horizontal axis (in Hz) and the wave power as the vertical axis. The time series has had a trend removed which was calculated by taking a running average over a window of 12.5 s. The top panel is for the Ly α channel, while the bottom panel is for the zirconium channel. The dotted line shows the spectral window that is used for filtering.

we have the axisymmetric modes: the fast sausage mode and the slow (sausage) mode. The fast sausage mode (also peristaltic mode) is a periodic transverse contraction and expansion of the cylinder, driven by the magnetic pressure. It operates on an Alfvén timescale. For long wavelengths (also slender loops), this mode becomes leaky and is damped by MHD radiation. The slow (sausage) mode is the typical coronal sound wave. It operates on a sound speed timescale, and induces density per-

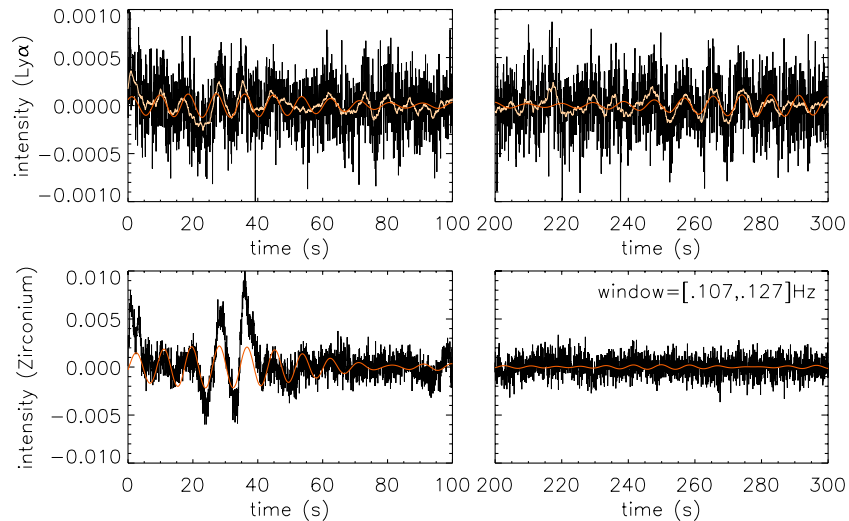


Figure 6. Black line is the de-trended intensity signal for the Ly α (top) and zirconium (bottom) channels. Overplotted in orange is the signal filtered for frequencies between 107 mHz and 127 mHz. Overlaid on the top panels in yellow is the smoothed time series (smoothing window of 50 data points or 2.5 s); this has not been used in the analysis and is shown for visual clarification only. The left panels are between $t = 0$ s and $t = 100$ s (i.e., onset and maximum of the flare in the Ly α channel); the right panels are from $t = 200$ s to $t = 300$ s in the decaying phase (in the Ly α channel) of the flare.

(A color version of this figure is available in the online journal.)

turbations traveling along the magnetic field, driven by the gas pressure. The latter two modes are the only modes with significant density (intensity) perturbations, and are therefore often used to explain QPPs.

Other possibilities also exist for the modulation of the intensity of the flare emission. Transverse oscillations are also known to sometimes have associated intensity variations (Wang & Solanki 2004; Aschwanden & Schrijver 2011). Since the mechanism responsible for this is not understood, we have not considered this option here. Also, more complicated emission mechanisms (e.g., gyrosynchrotron emission) depend on more parameters than the density alone, and may introduce intensity variations for other modes.

In our observations, we thus interpret the observed intensity oscillations as the fast sausage mode and the slow sausage mode, because these modes are the only ones with a significant compressibility. Furthermore, we use the periods to allow for classification of the modes: the longer period is considered as the slow mode and the shorter period is interpreted as the fast sausage mode. Also in earlier work, the long-period oscillations have classically been identified as slow mode oscillations in the flaring loop (e.g., Mariska 2005, but they have somewhat longer periods). The short-period oscillations are most often identified as the fast sausage mode (e.g., Melnikov et al. 2005, also with periods around 10 s), that are non-leaky in a short, fat flaring loop (Aschwanden et al. 2004). Both types of oscillations have been previously observed in solar flares. However, this is the first time that the two oscillation modes are observed simultaneously.

The simultaneous occurrence of two modes is decisive for performing improved coronal seismology. For example, in a review by Andries et al. (2009) it is explained that two fast kink mode longitudinal harmonics can be used to obtain results on the structuring of the loop along the magnetic field. In general, the more modes that are observed, the more information about the waveguide can be obtained.

To perform seismology, we assume that the two waves are both fundamental (i.e., only velocity nodes at the footpoints of the loop, later denoted as $n_s = n_f = 1$ where n is the number of half-wavelengths along the loop) $m = 0$ modes (fast sausage and slow) in the same structure. Thus, we assume that the wavelength and waveguide are identical for both modes. This assumption is reasonable since the observed emission contains both wave modes and the observed emission likely comes from one structure brightened by the flare energetic particles. The assumption of an identical wavelength is stringent, since it has been pointed out by Aschwanden et al. (2004) that the sausage modes may only be non-leaky near the top of the loop.

We consider the classical model for the waveguide: an overdense cylinder aligned with the magnetic field. The eigenmode structure for this configuration is well known (Nakariakov & Verwichte 2005). The density and magnetic field are homogeneous inside and outside the cylinder, but with different values. The internal (external) values are denoted with a subscript i (e). We assume a pressure balance between the internal and external region:

$$p_i + \frac{B_i^2}{2\mu} = p_e + \frac{B_e^2}{2\mu}, \quad (1)$$

where p is the gas pressure, B is the magnetic field magnitude, and μ is the permeability. It is possible that the condition of pressure balance is violated during the flare, because the flare is inherently dynamic and is not in equilibrium. Equation (1) may be rewritten in terms of characteristic speeds (e.g., Inglis et al.

2009):

$$\frac{\rho_e}{\rho_i} = \frac{2C_{si}^2 + \gamma C_{Ai}^2}{2C_{se}^2 + \gamma C_{Ae}^2}, \quad (2)$$

where ρ is the density, $C_s^2 = \gamma p / \rho$ is the square of the sound speed, $C_A^2 = B^2 / \mu \rho$ is the square of the Alfvén speed, and $\gamma = 5/3$ is the ratio of specific heats. For future reference, it is useful to rewrite this equation as follows:

$$\frac{C_{Ae}^2}{C_{Ai}^2} = \zeta \frac{\beta_i + 1}{\beta_e + 1}, \quad (3)$$

where $\beta = 2\mu p / B^2$ is the plasma- β (ratio of gas pressure to magnetic pressure) and $\zeta = \rho_i / \rho_e > 1$ is the density contrast. Since the loop is overdense, the density contrast ζ is taken to be larger than 1.

Short-wavelength limit. In the short-wavelength limit (i.e., short, fat loops, or $n \rightarrow \infty$), the phase speed of the slow sausage wave is the internal sound speed C_{si} , while the phase speed for the fast sausage mode is the internal Alfvén speed C_{Ai} (see, e.g., Nakariakov & Verwichte 2005, and references therein). Let us assume in a first simplification that both oscillations present fundamental modes ($n_s = n_f = 1$). Writing down that the loop length (wavelength) is identical for both waves yields:

$$75 \text{ s } C_{si} = 8.5 \text{ s } C_{Ai}, \quad (4)$$

where we have taken the average period for the long-period oscillation of the three LYRA channels. This equation can be transformed to give $\beta_i = \frac{2}{\gamma r} = 0.14$, where we have defined $r = 8.8$ as the ratio of the long period and the short period. The short-wavelength limit scenario is quite unlikely. While post-flare loops are short and fat, they are still loops. To have this short-wavelength limit, one needs higher harmonics of the fast sausage and slow sausage modes (at least $n > 10$). These are unlikely to be excited by a large-scale flare. Broadband drivers are more likely to excite the fundamental (with respect to the longitudinal direction) mode than high harmonics.

Long-wavelength limit. The long-wavelength limit (i.e., long, slender loops) cannot be considered rigorously, because the fast sausage mode is leaky in that case. Instead, let us consider wavelengths where the phase speed of the fast sausage mode is sufficiently close to the external Alfvén speed C_{Ae} . For these wavelengths, the phase speed of the slow mode is approximately the tube speed $C_T = C_A C_s / \sqrt{C_A^2 + C_s^2}$. The equivalent to Equation (4) that expresses the equality of wavelength for the two modes is then

$$75 \text{ s } C_{Ti} = 8.5 \text{ s } C_{Ae}, \quad (5)$$

which can be rearranged (using the expression for the tube speed) to

$$r = \frac{C_{Ae}}{C_{Ai}} \sqrt{1 + \frac{C_{Ai}^2}{C_{si}^2}}, \quad (6)$$

where r is the period ratio, as defined in the previous paragraph. Now we can use the condition of pressure balance (Equation (3)) to obtain

$$r^2 (\beta_e + 1) = \zeta (\beta_i + 1) \left(\frac{2}{\gamma \beta_i} + 1 \right). \quad (7)$$

This equation can be seen as a functional relationship between the plasma- β β_i and the density contrast ζ (at least when the

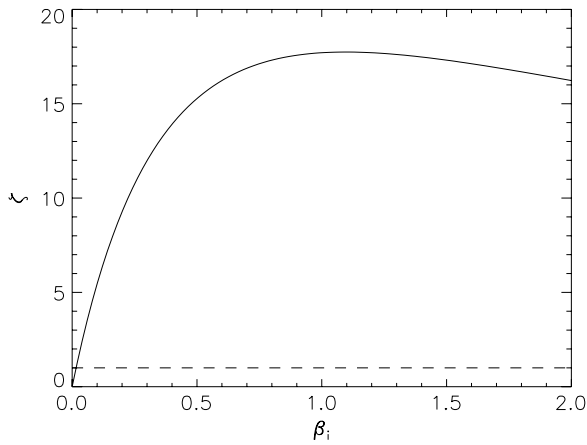


Figure 7. Functional relation (Equation (7)) between the plasma- β β_i and the density contrast ζ . β_e is taken as 0. The dashed line indicates the boundary $\zeta = 1$ for overdense loops.

external plasma- β β_e is considered as a parameter). It contains useful seismological information (see Figure 7).

The presence of the external plasma- β β_e hampers the straightforward solution of Equation (7). However, since the external plasma is not very much heated by the flare and the energetic particles, the external plasma- β can be considered to have the same value as the active region, i.e., of the order of a few percent. For clarity's sake, let us assume that $\beta_e \approx 0$ in order to show the seismological information contained in Equation (7). Later on, we will estimate the influence of the variation of this parameter.

The function $\zeta(\beta_i)$ (Equation (7)) is shown in Figure 7. First of all, it is obvious that the function has a maximum at $\beta_i = \sqrt{2/\gamma}$, where $\zeta_{\max} = r^2/(\sqrt{2/\gamma} + 1)^2 \approx 18$. We have thus found that the maximum density contrast in this flaring loop is at most $\zeta_{\max} = 18$, irrespective of the internal plasma- β . Looking at Figure 2 of Aschwanden et al. (2004), this maximum value of the density contrast can also be used to obtain an upper limit to the aspect ratio of the flaring loop. In this case, it is found that $(l/w)_{\text{SEIS}} \lesssim 2.5$, where l is the length of the loop and w is the loop diameter. This is not compatible with the assumption that we are in the long-wavelength limit.

Second, the constraint that $\zeta > 1$ (i.e., that the flaring loop is overdense) is only fulfilled for a certain range of plasma- β β_i . From Equation (7), it is easy to find that $\zeta = 1$ for $\beta_{i,\min} = \frac{2/\gamma}{r^2 - 2/\gamma - 1} \approx 0.016$ and $\beta_{i,\max} = r^2 - 2/\gamma - 1 - \beta_{i,\min} \approx 75$. We have thus found a minimum value for the plasma- β in this flaring loop. We have also found a maximum for the plasma- β , but this is less useful because the value is rather high. This is the first time that constraints on the plasma- β are found in flaring coronal loops.

Let us now have a look at the influence of the external plasma- β (which was assumed to be zero in the previous two paragraphs). In Equation (7) it can be seen that the factor r^2 is multiplied by $(1 + \beta_e)$. It is thus straightforward to add this factor in the results of the two previous paragraphs: $\zeta_{\max} = r^2(1 + \beta_e)/(\sqrt{2/\gamma} + 1)^2$ and $\beta_{i,\min} = \frac{2/\gamma}{r^2(1 + \beta_e) - 2/\gamma - 1}$. The value of the external plasma- β increases the maximum allowed density contrast, with a linear dependence. For example, for an external plasma- β of 5%, the maximum density contrast ζ_{\max} will also increase by 5%. On the other hand, the value of the external plasma- β will decrease the minimum of the internal plasma- β range. Since $r^2 \gg 1$, it can be understood that the

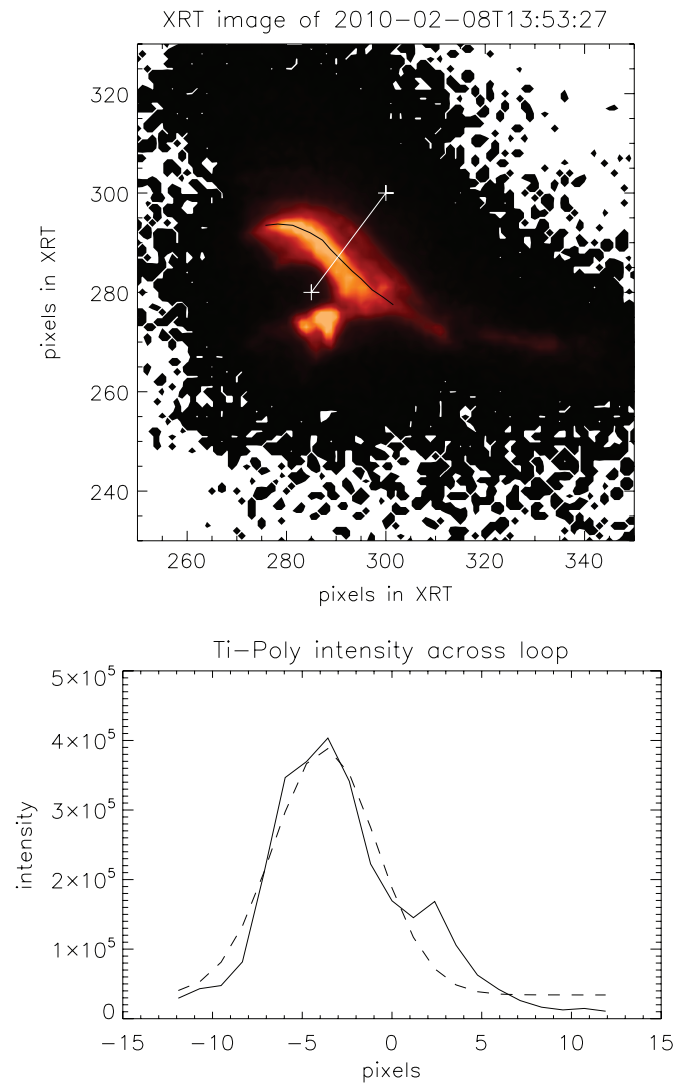


Figure 8. Top: image taken by *Hinode*/XRT just after the flare. The color scale indicates intensity. The black line indicates the flaring loop. Bottom: the full line shows the intensity across the loop, i.e., along the white line shown in the top panel. The dashed line is a Gaussian fit to the data.

(A color version of this figure is available in the online journal.)

value of the minimum internal plasma- β $\beta_{i,\min}$ decreases by 5% when the external plasma- β is 5%.

To test and better constrain the values inferred above, we try to directly observe the flaring loop.

Measurements of *Hinode*/XRT. The flare has also been observed with the *Hinode*/X-ray telescope (XRT) instrument. In Figure 8 (top panel) an image is shown taken just after the flare at 13:53UT. We have interpreted the bright ridge in the XRT image as the post-flare loop. However, since the time resolution of XRT is much too slow to observe the oscillations, it is observationally not proven that this is the oscillating loop. In addition, it is also possible that the loop extends to the lower left footpoint, instead of along the black line. However, in this case, the loop aspect ratio does not change very much.

In the XRT data, we have measured the length of the loop (indicated by the black line, which has been manually traced out). The width of the loop has been measured over the cross-section indicated by the white line. The intensity along this line has been displayed in the bottom panel of Figure 8. It can be seen in the cross-section that the flare loop is quite monolithic.

On this panel, we have overplotted the Gaussian fit which has been used for the measurement of the width. We have measured that the projected $(l/w)_{\text{POS}} = 4.6$, using the FWHM as a measure for the width. This is not compatible with the earlier inferred aspect ratio of the loop $((l/w)_{\text{SEIS}} = 2.5)$, and means that the previous models are not sufficiently refined.

However, since we now have more information, more refined seismology can be carried out. Let us first generalize Equation (4). The relationship between the wavenumbers of the fast mode and the slow mode (assuming that they live in the same post-flare loop) can generally be written as

$$n_s V_s P_s = n_f V_f P_f, \quad (8)$$

where n is the number of half-wavelengths along the loop (for example $n = 1$ is the fundamental mode), V is the phase speed, P is the period of the wave, and subscript s (f) refers to the slow (fast) mode. Equations (4) and (5) have specifically been calculated for $n_s = n_f = 1$.

The above equation can be rewritten as

$$r = \frac{P_s}{P_f} = \frac{n_f V_f}{n_s V_s}. \quad (9)$$

The left-hand side of this equation has been measured from the LYRA observations. The right-hand side can be calculated from MHD wave theory. In this paragraph we will consider the measured aspect ratio as a fixed quantity, in between the two limiting cases of the two previous paragraphs.

Since there are no analytical expressions for the fast sausage mode frequency and its dependence on the plasma- β and density contrast ζ , we have to numerically solve the dispersion relation for sausage waves ($m = 0$) in a magnetic-field-aligned overdense cylinder (Equation (8) in Edwin & Roberts 1983, with ka as a notation for the aspect ratio of the loop). In the calculations, we take $ka = n_{s,f}(l/w)_{\text{POS}} = 4.6n_{s,f}$, which assumes a semicircular loop shape.

From the numerical results, we find that the influence of the density contrast on the frequency of the fast and slow sausage modes is negligible. The only influence it has on the fast sausage mode is the introduction of the cutoff, where this mode becomes leaky. In our case, we consider a fixed ka (since this has been observed), and the presence of the cutoff introduces a minimum value for the density contrast ζ_{min} . For $n_f = \{1, 2, 3\}$, we find $\{\zeta_{\text{min},1} > 120, \zeta_{\text{min},2} > 30, \zeta_{\text{min},3} > 14\}$. However, these minimum values depend strongly on the plasma- β , i.e., when β increases, ζ_{min} increases drastically as well. In what follows, we consider $\zeta = 200$ in order to be well above the cutoff values for the density contrast. This seems to be in contrast to the earlier value of $\zeta_{\text{max}} = 18$, but that value would limit $n_f \leq 3$. In any case, the value of ζ does not influence the results of the numerical calculation very much.

The results of the calculations are shown in Figure 9, where we have plotted the right-hand side of Equation (9) versus the plasma- β (the influence of a variable ζ is negligible on this curve). The graph shows the nine curves for each possible combination of $\bigcup\{n_s, n_f\} = \{1, 2, 3\} \otimes \{1, 2, 3\}$.

It can be seen that the three curves for a fixed n_s (e.g., curves with diamonds) all occupy a relatively narrow range of period ratios. This shows that $n_f V_f$ does not vary a lot for different n_f . When performing seismology using these results, it will be nearly impossible to determine the fast sausage mode overtone number, since the fast overtone number does not influence the result much. However, in this respect, the cutoff values for the

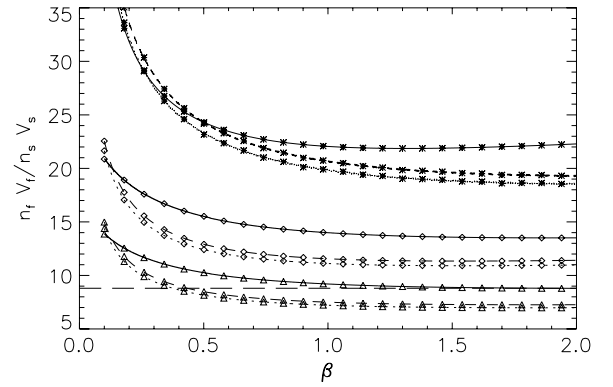


Figure 9. Theoretically predicted ratio of the slow mode and the fast mode period P_s/P_f as a function of the plasma- β , for a fixed density contrast of $\zeta = 200$. Solid lines are for $n_f = 1$, dotted for $n_f = 2$, and dashed for $n_f = 3$. Stars are for $n_s = 1$, diamonds for $n_s = 2$, and triangles for $n_s = 3$. The horizontal, long dashed line shows the observed value of $r = 8.8$.

density contrast may give a clue: while a density contrast of $\zeta_{\text{min},1} > 120$ is perhaps plausible in a post-flare loop, it certainly seems very high, making a mode number of $n_f = 1$ highly unlikely, unless leaky modes are considered.

In order to accommodate the observed value of $r = P_s/P_f = 8.8$, it is necessary to consider $n_s \geq 3$, since all the other values do not reproduce the observed period ratio. Once again, we find that the fundamental fast sausage mode $n_f = 1$ is a highly unlikely scenario, because this would require a plasma- $\beta \sim 1.5$. On the other hand, the first and second overtone fast sausage modes $n_f = 2, 3$ yield a plasma- β of 0.38 and 0.43, respectively, much more in line with the expected values.

We have not considered the leaky regime for the fast sausage mode, since it is outside the scope of this paper. Perhaps calculating the complex frequencies of the leaky fast sausage mode alleviates some of the problems with the fundamental mode (see above). It would allow for much more realistic values for the density contrast. The behavior of the fast sausage mode in this regime is not well understood.

To come to the above seismological estimates, it was necessary to make two important assumptions.

1. *Identical waveguide for both waves.* A strong assumption is that the two oscillation modes exist in the same post-flare loop waveguide. While it is unlikely that the oscillatory signal comes from another part of the Sun, it may be that two neighboring or overlying post-flare loops each support a different oscillation.
2. *Pressure balance for the post-flare loops.* We have assumed that the post-flare loops are in pressure equilibrium. This is likely not the case (since a flare is dynamic and post-flare loops evolve), but one may say that the flare evolution is slower than the timescale of the wave.

4. CONCLUSIONS

We have studied LYRA data during the M2.0 flare of 2010 February 8. In these data, we have found oscillatory signatures. We have observed long-period oscillations (period of ~ 75 s) in the zirconium, aluminum, and Ly α filters of the LYRA instrument. We have interpreted this oscillation as the standing slow sausage mode in the flaring loop.

We have also found short-period oscillations (period of ~ 8.5 s) which lasted the whole duration of the flare in the Ly α filter, but was only visible in the rising phase of the flare

in the zirconium filter. This short-period oscillation has been interpreted as the standing fast sausage mode. We thus observe two oscillation modes simultaneously in the same structure (in this case the flaring loop), showing great promise for performing coronal seismology.

To perform seismology, we have considered three different wavelength limits. In the first two cases, we have concentrated on extreme and rather unrealistic limiting cases. The last case takes an observational estimate of the loop aspect ratio.

1. *Short-wavelength limit.* Assuming that the wavelength of both waves is equal, we find the plasma- β to be 0.14.
2. *Long-wavelength limit.* Again assuming that the wavelength of both waves is equal, we can find an upper limit to the density contrast $\zeta_{\max} = 18$ of the flaring loop, and a lower limit to the plasma- β $\beta_{i,\min} = 1.6\%$ of the flaring loop. Using results from Aschwanden et al. (2004), an upper limit for the aspect ratio $l/w \lesssim 2.5$ of the flaring loop may also be found. This is in conflict with the long-wavelength limit.
3. *Measurement of the aspect ratio of the flare loop.* Using the XRT observations just after the flare, we have estimated the aspect ratio to be $(l/w)_{\text{POS}} = 4.6$. We use this value to calculate the wave phase speeds numerically. We find that the number of half-wavelengths of the slow wave along the loop has to be at least 3 to match the observed ratio of periods, when we limit the analysis to non-leaky wave modes. We find that the number of half-wavelengths of the fast mode must be at least 2, and that the plasma- β is 4 in this case.

For the first time, we have used coronal seismology in a flaring loop to constrain the density contrast, the plasma- β , and the mode numbers. The presence and measurement of the two oscillation modes in the high-cadence LYRA observations have allowed us to estimate physical parameters in flares which are not easily measured directly (due to, e.g., the lack of temporal and/or spatial resolution in other instruments). To perform seismology, it has been necessary to assume a geometry and pressure balance for the flaring region, and that the observed waves propagate in the same post-flare loop.

T.V.D. is funded by the “Return Grant” of the Belgian Science Policy. He thanks Professor Valery Nakariakov for useful comments. M.G. acknowledges support from GOA2009-009. LYRA is a project of the Centre Spatial de Liège, the Physikalisch-Meteorologisches Observatorium Davos, and the Royal Observatory of Belgium funded by the Belgian Federal

Science Policy Office (BELSPO) and by the Swiss Bundesamt für Bildung und Wissenschaft.

Facilities: PROBA2 (LYRA), Hinode (XRT)

REFERENCES

- Andries, J., Arregui, I., & Goossens, M. 2005a, *ApJ*, **624**, L57
- Andries, J., Goossens, M., Hollweg, J. V., Arregui, I., & Van Doorsselaere, T. 2005b, *A&A*, **430**, 1109
- Andries, J., Van Doorsselaere, T., Roberts, B., et al. 2009, *Space Sci. Rev.*, **149**, 3
- Arregui, I., Andries, J., Van Doorsselaere, T., Goossens, M., & Poedts, S. 2007, *A&A*, **463**, 333
- Asai, A., Shimojo, M., Isobe, H., et al. 2001, *ApJ*, **562**, L103
- Aschwanden, M. J., Nakariakov, V. M., & Melnikov, V. F. 2004, *ApJ*, **600**, 458
- Aschwanden, M. J., Nightingale, R. W., Andries, J., Goossens, M., & Van Doorsselaere, T. 2003, *ApJ*, **598**, 1375
- Aschwanden, M. J., & Schrijver, C. J. 2011, *ApJ*, **736**, 102
- Bárta, M., Vršnak, B., & Karlický, M. 2008, *A&A*, **477**, 649
- Benmoussa, A., Dammasch, I. E., Hochedez, J., et al. 2009, *A&A*, **508**, 1085
- De Moortel, I., & Brady, C. S. 2007, *ApJ*, **664**, 1210
- Edwin, P. M., & Roberts, B. 1983, *Sol. Phys.*, **88**, 179
- Fárník, F., Karlický, M., & Švestka, Z. 2003, *Sol. Phys.*, **218**, 183
- Fletcher, L., & Hudson, H. S. 2008, *ApJ*, **675**, 1645
- Gantois, K., Santandrea, S., Teston, F., et al. 2010, *ESA Bull.*, **144**, 23
- Goossens, M., Andries, J., & Aschwanden, M. J. 2002, *A&A*, **394**, L39
- Goossens, M., Arregui, I., Ballester, J. L., & Wang, T. J. 2008, *A&A*, **484**, 851
- Halain, J.-P., Berghmans, D., Defise, J.-M., et al. 2010, *Proc. SPIE*, **7732**, 77320P
- Hochedez, J., Schmutz, W., Stockman, Y., et al. 2006, *Adv. Space Res.*, **37**, 303
- Inglis, A. R., & Nakariakov, V. M. 2009, *A&A*, **493**, 259
- Inglis, A. R., Van Doorsselaere, T., Brady, C. S., & Nakariakov, V. M. 2009, *A&A*, **503**, 569
- Mariska, J. T. 2005, *ApJ*, **620**, L67
- McAteer, R. T. J., Gallagher, P. T., Brown, D. S., et al. 2005, *ApJ*, **620**, 1101
- Melnikov, V. F., Reznikova, V. E., Shibasaki, K., & Nakariakov, V. M. 2005, *A&A*, **439**, 727
- Nakariakov, V. M., Foullon, C., Myagkova, I. N., & Inglis, A. R. 2010, *ApJ*, **708**, L47
- Nakariakov, V. M., Foullon, C., Verwichte, E., & Young, N. P. 2006, *A&A*, **452**, 343
- Nakariakov, V. M., & Melnikov, V. F. 2009, *Space Sci. Rev.*, **149**, 119
- Nakariakov, V. M., & Ofman, L. 2001, *A&A*, **372**, L53
- Nakariakov, V. M., & Verwichte, E. 2005, *Living Rev. Sol. Phys.*, **2**, 3
- Pouget, G., Bocchialini, K., & Solomon, J. 2006, *A&A*, **450**, 1189
- Régner, S., Solomon, J., & Vial, J. C. 2001, *A&A*, **376**, 292
- Van Doorsselaere, T., Birtill, D. C. C., & Evans, G. R. 2009, *A&A*, **508**, 1485
- Van Doorsselaere, T., Brady, C. S., Verwichte, E., & Nakariakov, V. M. 2008, *A&A*, **491**, L9
- Van Doorsselaere, T., Wardle, N., Del Zanna, G., et al. 2011, *ApJ*, **727**, L32
- Veronig, A. M., Brown, J. C., Dennis, B. R., et al. 2005, *ApJ*, **621**, 482
- Verwichte, E., Nakariakov, V. M., Ofman, L., & Deluca, E. E. 2004, *Sol. Phys.*, **223**, 77
- Wang, T. J., & Solanki, S. K. 2004, *A&A*, **421**, L33
- Zimovets, I. V., & Struminsky, A. B. 2009, *Sol. Phys.*, **258**, 69